A Linear Least-Squares Solution to Elastic Shape-from-Template

Abed Malti[1] Adrien Bartoli[2] Richard Hartley[3]
[1] Fluminance/INRIA, Rennes, France
[2] ALCoV/ISIT, UMR 6284 CNRS/Université d'Auvergne, Clermont-Ferrand, France
[3]Australian National University and NICTA, Canberra, Australia

Abstract

We cast SfT (Shape-from-Template) as the search of a vector field $(\mathbf{X}, \delta\mathbf{X})$, composed of the pose $\mathbf{X}$ and the displacement $\delta\mathbf{X}$ that produces the deformation. We propose the first fully linear least-squares SfT method modeling elastic deformations. It relies on a set of Solid Boundary Constraints (SBC) to position the template at $\mathbf{X}$ in the deformed frame. The displacement is mapped by the stiffness matrix to minimize the amount of force responsible for the deformation. This linear minimization is subjected to the Reprojection Boundary Constraints (RBC) of the deformed shape $\mathbf{X} + \delta\mathbf{X}$ on the deformed image. Compared to state-of-the-art methods, this new formulation allows us to obtain accurate results at a low computational cost.

1. Introduction

The SfT problem is to reconstruct a 3D deformed surface from its image and a 3D shape template. Most SfT methods rely on point correspondences between the template and the image, defining Reprojection Boundary Constraints (*RBC*). These constrain 3D points to lie on the sightlines from the image, leaving an infinite number of possible 3D deformations. Physics-based or statistics-based priors are then used as additional constraints. In physics-based priors, the geometric and mechanical priors are the most used. While geometric priors tend to use invariant measures between deformations, mechanical priors represent the physics that rules the deformation. In parallel to an extensive study of isometry-based priors [3, 5, 17, 15, 18, 19], mechanical priors [1, 2, 10, 7] have recently become a line of investigation in SfT. They have potential for real applications since they address a wider class of deformable objects such as organs, tissues and other elastic objects. In comparison, isometric SfT is limited to paper and some types of clothes.

Current geometric/mechanical SfT methods suffer from a certain number of caveats that are summarized in table 1. First, the types of deformations: geometric approaches [3, 9] may not behave well when the prior is not fulfilled by the deformation, while mechanical methods [10, 1] cover a larger range of deformations (such as linear elasticity). Second, the tradeoff between accuracy and speed of estimation. Analytical solutions [3] are fast but with lower accuracy. Non-linear optimization methods [9, 10] are more accurate but at a higher computational cost. Moreover, their accuracy depends on the initialization and on some hyper-parameters. Methods based on Kalman filtering [1] also require an initialization step besides the fact that errors may accumulate over the considered time frame. In summary, physics-based approaches lack a method which is *(i)* able to exploit the mechanical constraints to cover a large deformation range, *(ii)* robust to noise, and *(iii)* both accurate and fast. Developing such a method is the main goal of this work. The answer we propose is to use mechanical constraints into a linear least-squares estimation framework.

We use finite elements (FEM) to represent the surface and the deformation. This is particularly adapted to SfT and fits the problem we want to solve. Indeed, only the finite discrete set of point correspondences has a natural boundary condition through the *RBC*. Any other point of the surface is free from boundary conditions and is only subject to the physical prior. Thus, we use the finite set of correspondences as nodes of the elements (triangles). Each element is subject to the mechanical laws that rule the deformation. We use a weak formulation of these laws to derive a linear relation (via the stiffness matrix) between the displacement of the nodes and the external deforming forces. The assembly of all elementary matrices reconstruct the global stiffness matrix that links the global external deforming force to the global deformation $\delta\mathbf{X}$. Minimizing this force subject to the *RBC* is a linear least-squares problem that can be solved very efficiently.

2. State-of-the-Art

Statistical constraints usually represent the deformation as a linear combination of basis vectors, which can be learned online either for face reconstruction [12] or for generic shapes [17, 15, 19]. Non-linear learning methods were applied in human tracking [16] and then extended to more generic surfaces [18].

Physical constraints include spatial and temporal surface priors. The isometry constraint [5] requires that any geodesic distance is preserved by the deformation. This approach has proven its accuracy for paper-like surfaces and was extended to conformal deformations [9, 3]. [3]

Method	Deformation			Time	Acc	Noise	Init/params
	Isometric	Conformal	Elastic				
analytic-GbM-[3]	+	+	−	+	−	−	+
iterative-GbM-[9]	+	+	−	−	+	+	−
iterative-MbM-[10]	+	+	+	−	+	+	−
sequential-MbM-[1]	+	+	+	+	−	+	−
linear-MbM-Proposed	+	+	+	+	+	+	+

Table 1. Strong (+) and weak (-) points of state-of-the-art physics-based SfT methods. GbM stands for geometric-based method and MbM for mechanics-based methods. **Time** is the computational cost. **Acc** is the accuracy of the method to recover the deformed shape. **Noise** is the sensitivity of the method to image noise. **Init/params** tells if the method requires an initial shape or hyper-parameters (-) or not (+). Isometric SfT methods are limited to isometric deformations and are not mentioned.

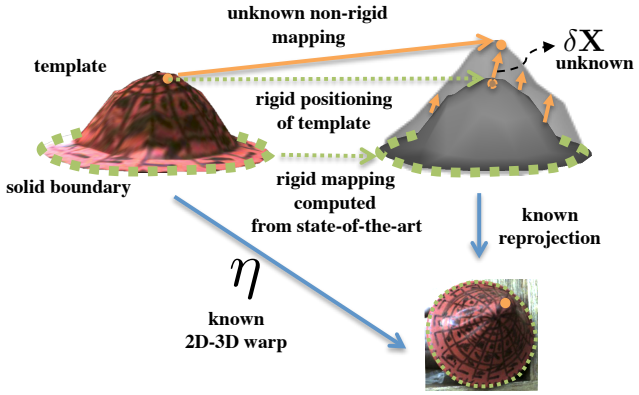

Figure 1. New formalization of the physics-based SfT. The displacement field at the solid boundary point is the zero 3-vector.

studied the well-posedness of both the isometric and conformal cases. The first SLAM (Simultaneous Localization And Mapping) method for elastic surfaces was attempted with fixed boundary conditions [1] and later extended to free boundary conditions [2]. This approach relies on the Navier-Stokes fluid-flow equation. It makes use of FEM to model the surface and approximates the deformation forces with Gaussians. Both the surface and the forces are estimated using an EKF (Extended Kalman Filter). It has to be noticed that SLAM and SfTare conceptually different. In the former a time sequential smoother is embedded in a Bayesian a-posteriori estimator. At the initialization the scene has to be static. Recently [10] proposed an SfTmethod with mechanical priors. The approach relies on stretching energy minimization under reprojection boundary conditions. [7] tested a similar approach with different mechanical models and orthographic projection. Though this has proven effective, it has the drawbacks of non-linear iterative methods: the need for an initialization (that is difficult to find) and for hyper-parameter setting to obtain an optimal accuracy.

FEM techniques with mechanical priors have been extensively used in medical imaging to solve organ segmentation from 3D volume scanning modalities [13, 20]. However these methods do not address the registration problem as is usually done in SfT.

3. Mathematical Formulation

Let n be the number of point correspondences. We propose to formalize SfT as follows: *find the 3D displacement field* $(\mathbf{X}, \delta\mathbf{X}) \in \mathbb{R}^{3n} \times \mathbb{R}^{3n}$*, where:* (i) $\delta\mathbf{X}$ *minimizes the norm of the applied forces for the deformation,* (ii) $\mathbf{X} + \delta\mathbf{X}$ *satisfies the RBC, and* (iii) $\mathbf{X}$ *is a rigid positioning of the template shape in the deformed frame thanks to the SBC.* See figure 1 for an illustration. Formally speaking, finding $(\mathbf{X}, \delta\mathbf{X})$ involves two main steps:

1. Find $\mathbf{X}$ from $\mathbf{X}_0$ with a PnP method applied to the solid boundary points of *SBC*. $\mathbf{X}_0$ is the template pose in the world coordinate frame.

2. Find $\delta\mathbf{X}$ such that:

$$\min_{\delta\mathbf{X}\in\mathbb{R}^{3n}} \frac{1}{2} \parallel \mathbf{K}\,\delta\mathbf{X} \parallel^2 \text{ s.t. } \begin{cases} \mathbf{P}\,\delta\mathbf{X} = \mathbf{b} & \textit{RBC} \\ \mathbf{S}\,\delta\mathbf{X} = \mathbf{0} & \textit{SBC} \end{cases} \quad (1)$$

Matrix $\mathbf{K}$ is the stiffness matrix of size $3n \times 3n$. Note that $\mathbf{f} = \mathbf{K}\,\delta\mathbf{X}$ is thus the vector of external forces to be minimized. $\mathbf{P}$ is an n-block diagonal matrix of dimension 2×3 per block. $\mathbf{P}$ and $\mathbf{b}$ enforce the fact that the n points must lie on the sightlines that pass through the n corresponding points in the deformed image. $\mathbf{S}$ is an $m \times 3n$ sparse matrix. It adds m depth displacement constraints which together with the corresponding $2m$, among $2n$, equations of *RBC* set the m solid boundary points. The construction of matrix $\mathbf{P}$ and vector $\mathbf{b}$ are straightforward. Consider a point $X + \delta X$ on the deformed shape and its reprojection $\eta = \begin{pmatrix}\eta_x & \eta_y\end{pmatrix}^\top$ in the image. The *RBC* for this point provides two non-homogeneous equations in the unknown point displacement $\delta X = \begin{pmatrix}u & v & w\end{pmatrix}^\top$. We use perspective projection and assume that the effect of the intrinsic parameters were undone on the image coordinates, which gives:

$$\begin{aligned} U + u &= \eta_x (W + w) \\ V + v &= \eta_y (W + w) \end{aligned} \quad (2)$$

or in matrix form as:

$$\underbrace{\begin{pmatrix} 1 & 0 & -\eta_x \\ 0 & 1 & -\eta_y \end{pmatrix}}_{P} \begin{pmatrix} u \\ v \\ w \end{pmatrix} = \underbrace{\begin{pmatrix} \eta_x W - U \\ \eta_y W - V \end{pmatrix}}_{b}, \quad (3)$$

where $X = \begin{pmatrix}U & V & W\end{pmatrix}^\top$. The global matrix $\mathbf{P}$ is written as:

$$\mathbf{P} = \begin{pmatrix} P^1 & \cdots & 0 & \cdots & 0 \\ 0 & \cdots & P^i & & 0 \\ 0 & \cdots & 0 & \cdots & P^n \end{pmatrix} \quad (4)$$

and $\mathbf{b}$ is written as:

$$\mathbf{b} = \begin{pmatrix} b^1 & \cdots & b^i & \cdots & b^n \end{pmatrix}^\top \quad (5)$$

The next sections are dedicated to the construction of matrix $\mathbf{K}$ with the related assumptions of deformation modeling.

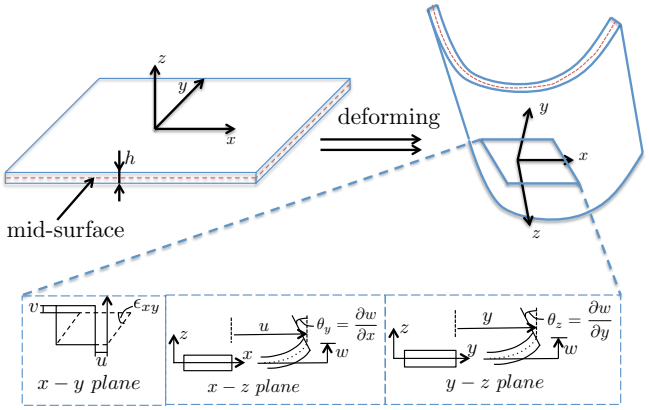

Figure 2. Local in-plane and out-of-plane deformations. To simplify the representation, we do not consider transverse shear in this example.

4. Mechanical Modeling

We adapt the plate theory [4] to surfaces which we assume have locally planar properties (2-manifolds). The equations of plate theory are written in local coordinates (tangent vectors and normal). Consider first a small flat surface, called the plate reference surface or simply the mid-surface Ω. We put a local coordinate system xyz on the mid-surface, x and y being the in-plane axes and z the out-of-plane axis. Extending $h/2$ above and $h/2$ below the z axis gives the whole surface with thickness h. The one in the $+z$ direction is by convention called the top surface (seen by the camera) whereas the one in the $-z$ direction is the bottom surface ($z = 0$ being the mid-surface). Such a three dimensional body is called a plate if the thickness h is everywhere small, but not too small, compared to a characteristic length L of the local plate mid-surface. The term small is to be interpreted in the engineering sense and not in the mathematical sense. For example, h/L is typically $1/5$ to $1/100$ for most plate structures.

Figure 2 illustrates the different variables of deforming an elementary plate. The local displacement $\delta X = \begin{pmatrix} u & v & w \end{pmatrix}^\top$ represents the deformation shift from an initial pose X. The mechanical laws applied to a deforming local plane relates this shift to the deforming forces. In what follows, we make explicit the physical relation between these variables and the deforming forces. In plane stress theory, both anisotropic scaling and shearing are taken into account. The equations of equilibrium relates the stress (internal body forces) to the external forces:

$$\begin{aligned} \frac{\partial \sigma_x}{\partial x} + \frac{\partial \sigma_{xy}}{\partial y} + \frac{\partial \sigma_{xz}}{\partial z} + f_x = 0 \\ \frac{\partial \sigma_{xy}}{\partial x} + \frac{\partial \sigma_y}{\partial y} + \frac{\partial \sigma_{yz}}{\partial z} + f_y = 0 \\ \frac{\partial \sigma_{xz}}{\partial x} + \frac{\partial \sigma_{yz}}{\partial y} + f_z = 0 \end{aligned} \tag{6}$$

where $\begin{pmatrix} f_x & f_y & f_z \end{pmatrix}^\top$ are the components of the external body forces per unit volume. σ_x, σ_y are the in-plane axial stress component. σ_{xy}, σ_{yz} and σ_{xz} are the shear stress components. For a thin material, the transverse axial stress σ_z is neglected since we assume that the thickness barely changes after deformation. These equations represent the combined bending and transverse shear deformation on thin materials. The bending stress components are $\begin{pmatrix} \sigma_x & \sigma_y & \sigma_{xy} \end{pmatrix}^\top$ and the transverse shear stress components are $\begin{pmatrix} \sigma_{xz} & \sigma_{yz} \end{pmatrix}^\top$. The bending behaviour is associated with in-plane deformations and the transverse shear behaviour is associated with the rotation of surface normals after deformation.

The constitutive equation provides the relationship between the stresses and strains. For a homogeneous and isotropic material, the in-plane stress-strain relation is:

$$\begin{pmatrix} \sigma_x \\ \sigma_y \\ \sigma_{xy} \end{pmatrix} = \underbrace{\frac{E}{1-\nu^2} \begin{pmatrix} 1 & \nu & 0 \\ \nu & 1 & 0 \\ 0 & 0 & \frac{1-\nu}{2} \end{pmatrix}}_{\mathbf{D}_b} \begin{pmatrix} \epsilon_x \\ \epsilon_y \\ \epsilon_{xy} \end{pmatrix}, \tag{7}$$

where ϵ_x, ϵ_y are the in-plane axial strain and ϵ_{xy} is the in-plane shear strain. E is Young's modulus and ν is Poisson's ratio. The transverse shear stress-strain relation is:

$$\begin{pmatrix} \sigma_{xz} \\ \sigma_{yz} \end{pmatrix} = \underbrace{\begin{pmatrix} \frac{E}{2(1+\nu)} & 0 \\ 0 & \frac{E}{2(1+\nu)} \end{pmatrix}}_{\mathbf{D}_s} \begin{pmatrix} \epsilon_{xz} \\ \epsilon_{yz} \end{pmatrix} \tag{8}$$

where ϵ_{xz} and ϵ_{yz} are the rotation angles about respectively the y and x axes of the local mid-surface caused by the transverse deformation. The in-plane strains are related to the displacement by what is called the in-plane kinematic equation:

$$\begin{pmatrix} \epsilon_x \\ \epsilon_y \\ \epsilon_{xy} \end{pmatrix} = \begin{pmatrix} \frac{\partial u}{\partial x} \\ \frac{\partial v}{\partial y} \\ \frac{\partial u}{\partial y} + \frac{\partial v}{\partial x} \end{pmatrix} \tag{9}$$

The transverse shear strains are related to the displacement by what is called the out-of-plane kinematic equation:

$$\begin{pmatrix} \epsilon_{xz} \\ \epsilon_{yz} \end{pmatrix} = \begin{pmatrix} \frac{\partial u}{\partial z} + \frac{\partial w}{\partial x} \\ \frac{\partial v}{\partial z} + \frac{\partial w}{\partial y} \end{pmatrix} \tag{10}$$

Combining all these mechanical equations results in a second order Partial Differential Equation (PDE) in the displacement vector. This PDE requires the displacement to be twice continuously differentiable. Moreover, using FEM with such an order is not as stable as for a first order since the computation would require second order derivations. For this reason, we derive a weak formulation at first order. This new obtained PDE requires the displacement to be continuously differentiable and can be easily handled by FEM.

5. Weak Formulation

The weak formulation method derives from distribution theory. First, it uses scalar products of the PDE with so

called test functions. Second, thanks to integration by parts, the derivatives on the unknowns are transported to test functions and boundary conditions are exhibited. Finally, after some appropriate manipulations, we end up with a first order PDE that can be represented easily with FEM.

5.1. Scalar Product with Test Functions

Multiplying equation (6) by the test functions $\begin{pmatrix}\alpha & \beta & \gamma\end{pmatrix}^\top$, we obtain:

$$\begin{aligned}\int_{-\frac{h}{2}}^{\frac{h}{2}}\int_\Omega \begin{pmatrix}\alpha\\ \beta\\ \gamma\end{pmatrix}^\top \begin{pmatrix}\frac{\partial\sigma_x}{\partial x}+\frac{\partial\sigma_{xy}}{\partial y}+\frac{\partial\sigma_{xz}}{\partial z}\\ \frac{\partial\sigma_{xy}}{\partial x}+\frac{\partial\sigma_y}{\partial y}+\frac{\partial\sigma_{yz}}{\partial z}\\ \frac{\partial\sigma_{xz}}{\partial x}+\frac{\partial\sigma_{yz}}{\partial y}\end{pmatrix} d\Omega\, dz+\\ \int_{-\frac{h}{2}}^{\frac{h}{2}}\int_\Omega \begin{pmatrix}\alpha\\ \beta\\ \gamma\end{pmatrix}^\top \begin{pmatrix}f_x\\ f_y\\ f_z\end{pmatrix} d\Omega\, dz=0,\end{aligned} \tag{11}$$

which is valid for any $\begin{pmatrix}\alpha & \beta & \gamma\end{pmatrix}\in\mathbb{R}^3$ that fits the *SBC*. Here, we denote $d\Omega = dx\,dy$. Splitting up the parts related to the bending and transverse shear deformations gives:

$$\begin{aligned}\int_{-\frac{h}{2}}^{\frac{h}{2}}\int_\Omega \begin{pmatrix}\alpha\\ \beta\end{pmatrix}^\top \begin{pmatrix}\frac{\partial\sigma_x}{\partial x}+\frac{\partial\sigma_{xy}}{\partial y}\\ \frac{\partial\sigma_{xy}}{\partial x}+\frac{\partial\sigma_y}{\partial y}\end{pmatrix} d\Omega\, dz+\\ \int_{-\frac{h}{2}}^{\frac{h}{2}}\int_\Omega \begin{pmatrix}\alpha\\ \beta\\ \gamma\end{pmatrix}^\top \begin{pmatrix}\frac{\partial\sigma_{xz}}{\partial z}\\ \frac{\partial\sigma_{yz}}{\partial z}\\ \frac{\partial\sigma_{xz}}{\partial x}+\frac{\partial\sigma_{yz}}{\partial y}\end{pmatrix} d\Omega\, dz+\\ \int_{-\frac{h}{2}}^{\frac{h}{2}}\int_\Omega \begin{pmatrix}\alpha\\ \beta\\ \gamma\end{pmatrix}^\top \begin{pmatrix}f_x\\ f_y\\ f_z\end{pmatrix} d\Omega\, dz=0.\end{aligned} \tag{12}$$

5.2. Integration by Parts

To remove the derivation on the bending stress and the transverse shear stress in equation (12), we use integration by parts:

$$\begin{aligned}\int_{-\frac{h}{2}}^{\frac{h}{2}}\int_\Omega \begin{pmatrix}\frac{\partial\alpha}{\partial x}\\ \frac{\partial\beta}{\partial y}\\ \frac{\partial\alpha}{\partial y}+\frac{\partial\beta}{\partial x}\end{pmatrix}^\top \begin{pmatrix}\sigma_x\\ \sigma_y\\ \sigma_{xy}\end{pmatrix} d\Omega\, dz+\\ \int_{-\frac{h}{2}}^{\frac{h}{2}}\int_\Omega \begin{pmatrix}\frac{\partial\alpha}{\partial z}+\frac{\partial\gamma}{\partial x}\\ \frac{\partial\beta}{\partial z}+\frac{\partial\gamma}{\partial y}\end{pmatrix}^\top \begin{pmatrix}\sigma_{xz}\\ \sigma_{yz}\end{pmatrix} d\Omega\, dz+\\ \int_{-\frac{h}{2}}^{\frac{h}{2}}\int_\Omega \begin{pmatrix}\alpha\\ \beta\\ \gamma\end{pmatrix}^\top \begin{pmatrix}f_x\\ f_y\\ f_z\end{pmatrix} d\Omega\, dz-\\ \int_{-\frac{h}{2}}^{\frac{h}{2}}\int_\Gamma \begin{pmatrix}\alpha\\ \beta\end{pmatrix}^\top \begin{pmatrix}N_x\\ N_y\end{pmatrix} d\Gamma\, dz-\\ \int_{-\frac{h}{2}}^{\frac{h}{2}}\int_\Gamma \begin{pmatrix}\alpha+\gamma\\ \beta+\gamma\end{pmatrix}^\top \begin{pmatrix}\sigma_{xz}n_z\\ \sigma_{yz}n_z\end{pmatrix} d\Gamma\, dz=0,\end{aligned} \tag{13}$$

where $\Gamma\times z$ is the boundary of $\Omega\times z$. $N_x=\sigma_x n_x+\sigma_{xy}n_y$ and $N_y=\sigma_{xy}n_x+\sigma_y n_y$ are the in-plane stress components at the boundaries. $\begin{pmatrix}\sigma_{xz}n_z & \sigma_{yz}n_z\end{pmatrix}$ are the transverse shear components related to the displacement at the boundaries and $\begin{pmatrix}n_x & n_y & n_z\end{pmatrix}^\top$ is the surface normal at the boundary points. Substituting the constitutive equation (7) in (13) gives:

$$\begin{aligned}\int_{-\frac{h}{2}}^{\frac{h}{2}}\int_\Omega \begin{pmatrix}\frac{\partial\alpha}{\partial x}\\ \frac{\partial\beta}{\partial y}\\ \frac{\partial\alpha}{\partial y}+\frac{\partial\beta}{\partial x}\end{pmatrix}^\top \mathbf{D}_b \begin{pmatrix}\epsilon_x\\ \epsilon_y\\ \epsilon_{xy}\end{pmatrix} d\Omega\, dz+\\ \int_{-\frac{h}{2}}^{\frac{h}{2}}\int_\Omega \begin{pmatrix}\frac{\partial\alpha}{\partial z}+\frac{\partial\gamma}{\partial x}\\ \frac{\partial\beta}{\partial z}+\frac{\partial\gamma}{\partial y}\end{pmatrix}^\top \mathbf{D}_s \begin{pmatrix}\epsilon_{xz}\\ \epsilon_{yz}\end{pmatrix} d\Omega\, dz+\\ \int_{-\frac{h}{2}}^{\frac{h}{2}}\int_\Omega \begin{pmatrix}\alpha\\ \beta\\ \gamma\end{pmatrix}^\top \begin{pmatrix}f_x\\ f_y\\ f_z\end{pmatrix} d\Omega\, dz-\\ \int_{-\frac{h}{2}}^{\frac{h}{2}}\int_\Gamma \begin{pmatrix}\alpha\\ \beta\end{pmatrix}^\top \begin{pmatrix}N_x\\ N_y\end{pmatrix} d\Gamma\, dz-\\ \int_{-\frac{h}{2}}^{\frac{h}{2}}\int_\Gamma \begin{pmatrix}\alpha+\gamma\\ \beta+\gamma\end{pmatrix}^\top \begin{pmatrix}\sigma_{xz}n_z\\ \sigma_{yz}n_z\end{pmatrix} d\Gamma\, dz=0.\end{aligned} \tag{14}$$

One more substitution of the kinematic equation (9) into (14) gives:

$$\begin{aligned}\int_{-\frac{h}{2}}^{\frac{h}{2}}\int_\Omega \begin{pmatrix}\frac{\partial\alpha}{\partial x}\\ \frac{\partial\beta}{\partial y}\\ \frac{\partial\alpha}{\partial y}+\frac{\partial\beta}{\partial x}\end{pmatrix}^\top \mathbf{D}_b \begin{pmatrix}\frac{\partial u}{\partial x}\\ \frac{\partial v}{\partial y}\\ \frac{\partial u}{\partial y}+\frac{\partial v}{\partial x}\end{pmatrix} d\Omega\, dz+\\ \int_{-\frac{h}{2}}^{\frac{h}{2}}\int_\Omega \begin{pmatrix}\frac{\partial\alpha}{\partial z}+\frac{\partial\gamma}{\partial x}\\ \frac{\partial\beta}{\partial z}+\frac{\partial\gamma}{\partial y}\end{pmatrix}^\top \mathbf{D}_s \begin{pmatrix}\epsilon_{xz}\\ \epsilon_{yz}\end{pmatrix} d\Omega\, dz=\\ -\int_{-\frac{h}{2}}^{\frac{h}{2}}\int_\Omega \begin{pmatrix}\alpha\\ \beta\\ \gamma\end{pmatrix}^\top \begin{pmatrix}f_x\\ f_y\\ f_z\end{pmatrix} d\Omega\, dz+\\ \int_{-\frac{h}{2}}^{\frac{h}{2}}\int_\Gamma \begin{pmatrix}\alpha\\ \beta\end{pmatrix}^\top \begin{pmatrix}N_x\\ N_y\end{pmatrix} d\Gamma\, dz+\\ \int_{-\frac{h}{2}}^{\frac{h}{2}}\int_\Gamma \begin{pmatrix}\alpha+\gamma\\ \beta+\gamma\end{pmatrix}^\top \begin{pmatrix}\sigma_{xz}n_z\\ \sigma_{yz}n_z\end{pmatrix} d\Gamma\, dz.\end{aligned} \tag{15}$$

Note that replacing $\begin{pmatrix}\alpha & \beta & \gamma\end{pmatrix}$ by $\begin{pmatrix}u & v & w\end{pmatrix}$ leads to a quadratic internal energy term on the left-hand side and an external energy term at the right-hand side. This equality states that the external energy spent on the deformation is fully transferred to the material.

5.3. Change of Variables: from local in-plane displacements to angles of rotation of the patch normal

Substituting the second kinematic equation (10) into (15) involves derivatives with respect to z. For thin plates,

computing such derivative can be very unstable. To overcome this, we propose a change of variable that will avoid computing these derivatives. The local displacements $\begin{pmatrix} u & v & w \end{pmatrix}^\top$ can be expressed with respect to the rotation of the patch normal. When the transverse shear is considered, the classic Kirchoff laws [4] can be extended to the following formulas:

$$\begin{aligned} u &= -z\,\theta_x(x,y), \\ v &= -z\,\theta_y(x,y), \\ w &= w(x,y), \end{aligned} \tag{16}$$

where θ_x and θ_y are local rotations about the tangent vectors y and x. For shear deformable plate, the relation between these angles and the normal displacement w is:

$$\begin{aligned} \theta_x &= \frac{\partial w}{\partial x} - \epsilon_{xz}, \\ \theta_y &= \frac{\partial w}{\partial y} - \epsilon_{yz}. \end{aligned} \tag{17}$$

Equations (16) and (17) illustrate the fact that a change of orientation of the patch normal is caused by both bending and transverse shear. In the case of only in-plane deformation (*e.g.* planar stretching), only the transverse shear may be responsible of the change in normal orientation. The test function being any function, the changes of variable on $\begin{pmatrix} u & v & w \end{pmatrix}^\top$ can be similarly applied to the test functions so that we obtain similar terms on the left and right hand sides of $\mathbf{D}_b$ and $\mathbf{D}_s$. Let us denote $\begin{pmatrix} \tilde{\alpha} & \tilde{\beta} & \gamma \end{pmatrix}^\top$ the new test functions obtained from the former test functions with similar changes of variable (16) and (17). Using these two changes of variables into (15) yields:

$$\begin{aligned} \int_{-\frac{h}{2}}^{\frac{h}{2}} \int_\Omega \begin{pmatrix} -z\frac{\partial \tilde{\alpha}}{\partial x} \\ -z\frac{\partial \tilde{\beta}}{\partial y} \\ -z(\frac{\partial \tilde{\alpha}}{\partial y} + \frac{\partial \tilde{\beta}}{\partial x}) \end{pmatrix}^\top \mathbf{D}_b \begin{pmatrix} -z\frac{\partial \theta_x}{\partial x} \\ -z\frac{\partial \theta_y}{\partial y} \\ -z(\frac{\partial \theta_x}{\partial y} + \frac{\partial \theta_y}{\partial x}) \end{pmatrix} d\Omega\, dz + \\ \int_{-\frac{h}{2}}^{\frac{h}{2}} \int_\Omega \begin{pmatrix} \frac{\partial \gamma}{\partial x} - \tilde{\alpha} \\ \frac{\partial \gamma}{\partial y} - \tilde{\beta} \end{pmatrix}^\top \mathbf{D}_s \begin{pmatrix} \frac{\partial w}{\partial x} - \theta_x \\ \frac{\partial w}{\partial y} - \theta_y \end{pmatrix} d\Omega\, dz = \\ -\int_{-\frac{h}{2}}^{\frac{h}{2}} \int_\Omega \begin{pmatrix} -z\tilde{\alpha} \\ -z\tilde{\beta} \\ \gamma \end{pmatrix}^\top \begin{pmatrix} f_x \\ f_y \\ f_z \end{pmatrix} d\Omega\, dz + \\ \int_{-\frac{h}{2}}^{\frac{h}{2}} \int_\Gamma \begin{pmatrix} -z\tilde{\alpha} \\ -z\tilde{\beta} \end{pmatrix}^\top \begin{pmatrix} N_x \\ N_y \end{pmatrix} d\Gamma\, dz + \\ \int_{-\frac{h}{2}}^{\frac{h}{2}} \int_\Gamma \begin{pmatrix} -z\tilde{\alpha} + \gamma \\ -z\tilde{\beta} + \gamma \end{pmatrix}^\top \begin{pmatrix} \sigma_{xz} n_z \\ \sigma_{yz} n_z \end{pmatrix} d\Gamma\, dz. \end{aligned} \tag{18}$$

Equation (18) constrains the solution $\begin{pmatrix} \theta_x & \theta_y & w \end{pmatrix}^\top$ to be continuously differentiable. This condition is weaker in term of regularity than the original equation (6) that imposes $\begin{pmatrix} u & v & w \end{pmatrix}^\top$ to be twice continuously differentiable. This weaker regularity has also the advantage to let the surface fold sharply if required.

6. Iso-Parametric FEM

We approximate the whole surface $\mathbf{\Sigma}$ with a mesh of triangle patches Ω^j, $1 \leq j \leq e$, where e is the number of patch elements. In order to use the FEM approach, we parameterize surface points and the corresponding displacements with shape functions [6]. We use iso-parametric shape functions to interpolate the surface points, the displacements and the test functions. If we consider a triangle patch, then the interpolation scheme is written as:

$$Q(\xi_1, \xi_2) = \sum_{i=1}^{n} S_i(\xi_1, \xi_2)\, Q^i,\ 1 \leq i \leq n, \tag{19}$$

where $(\xi_1, \xi_2) \in \mathbb{R}^2$ is a global parameterization. Q is a mute variable that can be replaced by the surface point X, the displacement w, θ_x, θ_y and the test functions $\tilde{\alpha}$, $\tilde{\beta}$, γ. $\{S_i(\xi_1, \xi_2)\}_{1 \leq i \leq n}$, are real valued differentiable functions called shape functions. The support of S_i is the union of patches that contains node i. The shape functions must sum to one for all ξ_1, ξ_2. $\Theta^i = \begin{pmatrix} \theta_x^i & \theta_y^i & w^i \end{pmatrix}^\top$ is the displacement of node i. $\tau^i = \begin{pmatrix} \tilde{\alpha}^i & \tilde{\beta}^i & \gamma^i \end{pmatrix}^\top$ are the values of the test functions at node i.

First we focus on the left-hand side of equation (18) that we denote $\mathcal{E}_l$. The right-hand side is denoted $\mathcal{E}_r$ and will be addressed right after. We replace the displacement and test function parameterization of equation (19) into $\mathcal{E}_l$ to obtain a global equation that uses the global bending stiffness $\tilde{\mathbf{K}}_b$ and the global transverse shear stiffness $\tilde{\mathbf{K}}_s$ matrices:

$$\mathcal{E}_l = \mathbf{T}^\top \left(\tilde{\mathbf{K}}_b + \tilde{\mathbf{K}}_s \right) \mathbf{\Theta} = \mathbf{T}^\top \tilde{\mathbf{K}} \mathbf{\Theta}, \tag{20}$$

where $\mathbf{\Theta} = \begin{pmatrix} \Theta^1 & \cdots & \Theta^n \end{pmatrix}^\top$ is the global displacement $3n$-vector and $\mathbf{T}$ is the global nodal test function $3n$-vector. $\tilde{\mathbf{K}}$ is the global stiffness matrix. $\tilde{\mathbf{K}}_b$ and $\tilde{\mathbf{K}}_s$ are the global bending and transverse shear stiffness matrices (the tilde symbol represents matrices related to the new variable $\mathbf{\Theta}$). They are assembled from bending and transverse shear stiffness matrices of each element patch:

$$\begin{aligned} \mathbf{k}_b &= \left(\int_{-\frac{h}{2}}^{\frac{h}{2}} \int_\Omega z^2\, \mathbf{B}_b^\top\, \mathbf{D}_b\, \mathbf{B}_b\, d\Omega\, dz \right) \\ \mathbf{k}_s &= \left(\int_{-\frac{h}{2}}^{\frac{h}{2}} \int_\Omega \mathbf{B}_s^\top\, \mathbf{D}_b\, \mathbf{B}_s\, d\Omega\, dz \right), \end{aligned} \tag{21}$$

with the formula:

$$\begin{aligned} \tilde{\mathbf{K}}_b(I,J) &= \sum_{k=1}^{e} \sum_{(I,J) \in \Omega^k} \mathbf{k}_b(i_I, j_J), \\ \tilde{\mathbf{K}}_s(I,J) &= \sum_{k=1}^{e} \sum_{(I,J) \in \Omega^k} \mathbf{k}_s(i_I, j_J), \end{aligned} \tag{22}$$

where $1 < I, J < 3n$ is the global indexing of node displacements and $1 \leq i_I, j_J \leq 3 \times 3$ is the corresponding local element indexing. The expressions of $\mathbf{B}_b$, $\mathbf{B}_s$ are easily obtained from the Jacobian matrices of shape functions when applied to Θ and test functions [6]. Applying the same reasoning to the right-hand side of equation (18), we can deduce a similar formula involving the external nodal force $\mathbf{f}$:

$$\mathcal{E}_r = \mathbf{T}^\top \mathbf{f}. \tag{23}$$

Thus, the approximation of equation (18) with FEM is:

$$\mathbf{T}^\top \tilde{\mathbf{K}}\, \mathbf{\Theta} = \mathbf{T}^\top \mathbf{f}, \text{ for all } \mathbf{T} \in \mathbb{R}^{3n} \tag{24}$$

For this equation to hold for any $\mathbf{T}$, we have obviously:

$$\tilde{\mathbf{K}}\, \mathbf{\Theta} = \mathbf{f} \tag{25}$$

In order to recover the initial global displacement vector $\delta\mathbf{X}$, we apply the inverse variable change, which gives:

$$\tilde{\mathbf{K}}\, \mathbf{H}\, \delta\mathbf{X} = \mathbf{K}\, \delta\mathbf{X} = \mathbf{f}. \tag{26}$$

where $\mathbf{H}$ is a $3n$ block diagonal matrix with blocks $H = \text{diag}\begin{pmatrix} -2/h, & -2/h, & 1 \end{pmatrix}$. Recall h is the material thickness and $z = h/2$ corresponds to the top surface of the material. Now we have seen the construction of matrix $\mathbf{K}$ and previously the construction of matrices $\mathbf{P}$ and $\mathbf{S}$. We can thus study the feasibility and uniqueness of solution for our SfT formulation (1).

7. Feasibility and Solution Uniqueness

By construction $\mathbf{K}$ is not always full rank especially if the elements are not regular. However, with sufficient m, $\mathbf{K}$ becomes full rank after adding the m *SBC*s as follows:

$$\begin{aligned} \mathbf{K}(3i, 3j) &= 1, \text{if } i = j \\ \mathbf{K}(3i, 3j) &= 0, \text{otherwise,} \end{aligned} \tag{27}$$

with i running only for *SBC* nodes and $1 \leq j \leq n$. Practically, we can add sufficient *SBC*s to make $\mathbf{K}$ full rank. To exhibit the feasibility and uniqueness of problem (1), we compute its Lagrangian:

$$\mathcal{L}(\delta\mathbf{X}, \lambda, \mu) = \frac{1}{2}\delta\mathbf{X}^\top \mathbf{K}^\top \mathbf{K}\, \delta\mathbf{X} + \lambda^\top (\mathbf{P}\delta\mathbf{X} - \mathbf{b}) + \mu^\top \mathbf{S}\delta\mathbf{X}, \tag{28}$$

where λ is a $2n$-vector and μ is an m-vector. The optimality conditions are written as:

$$\frac{\partial \mathcal{L}}{\partial \delta\mathbf{X}} = \mathbf{K}^\top \mathbf{K}\, \delta\mathbf{X} + \mathbf{C} \begin{pmatrix} \lambda^\top & \mu^\top \end{pmatrix}^\top = 0, \tag{29}$$

$$\frac{\partial \mathcal{L}}{\partial (\lambda, \mu)} = \mathbf{C}\, \delta\mathbf{X} = \begin{pmatrix} \mathbf{b}^\top & 0 \end{pmatrix}^\top, \tag{30}$$

with $\mathbf{C} = \begin{pmatrix} \mathbf{P}^\top & \mathbf{S}^\top \end{pmatrix}^\top$ a matrix of rank $2n + m$ by construction. The set of feasible solutions δX is written as

$$\widehat{\delta\mathbf{X}} = \overline{\delta\mathbf{X}} + \mathbf{d}, \tag{31}$$

where $\overline{\delta X}$ is any vector that satisfies (30) and $\mathbf{d} \in \text{Ker}\{C\}$ (the null space of $\mathbf{C}$). Substituting in (28) we find:

$$\mathbf{K}^\top \mathbf{K}\, \mathbf{d} = -\mathbf{K}^\top \mathbf{K}\, \overline{\delta\mathbf{X}} - \mathbf{C} \begin{pmatrix} \lambda \\ \mu \end{pmatrix} \tag{32}$$

This equation has a unique solution if and only if the restriction of $\mathbf{K}^\top \mathbf{K}$ to $\text{Ker}\{C\}$ is invertible. This is the case since $\mathbf{K}$ is full rank by construction and by equation (27).

8. Experimental Results

8.1. Compared Methods

To have a representative evaluation with related state-of-the-art methods, we compare our method **LM** (linear mechanics-based) to four other methods that have been presented previously in section 2 and table 1: *(1)* **NLM** [10], a non-linear iterative method that minimizes stretching energy. *(2)* **KFM** [1], a sequential method that uses mechanical priors embedded in a Kalman Filtering process. *(3)* **NLG** [9], a non-linear iterative method that minimizes a local isotropy penalty. *(4)* **AG** [3], an analytic geometric method that uses local isotropy as prior.

These methods were evaluated using MATLAB R2014A on a MAC desktop (OS X 10.9.5) with QUAD-CORE INTEL XEON running at 2×2.66 GHz. Our evaluation is based on three criteria: *(i)* accuracy, *(ii)* computation time and *(iii)* robustness to image noise for the synthetic experiments. The amount of extensibility ϵ is expressed as a percentage of the relative variation of the stretching energy with respect to the ground-truth template [10].

8.2. Simulated Data

The synthetic deformations are obtained using *3D Studio Max* [11]. This provides plausible deformations according to the mechanical properties of the considered material. We simulate a material with Poisson's ratio $\nu = 0.49$ and Young's modulus $E = 10^6$ Pa (Pa stands for Pascals to measure force per unit area). Such a material deforms like a toy balloon for $\epsilon \leq 15\%$. We use a planar template of size 150×150 mm^2. We subdivide it in a regular grid of $N = 30 \times 30$ nodes and 1682 triangular faces. The largest length of each triangle being $5\sqrt{2}$ mm, we choose a thickness $h = 0.8$ mm such that it fits the local plate assumption (*c.f.* section 4). The points at the boundary of the material are taken as being part of the *SBC*. The deforming forces are applied at the nodes of the grid. Their magnitude follows a gaussian distribution of standard deviation of 20 Newton and their orientations vary from node to node with a uniform distribution. To obtain the deformed images, the nodes on the simulated deformed surfaces are projected with a calibrated perspective camera located 800 mm from the surface. We run two sets of test; *(i)* Robustness to noise: centred Gaussian noise $\mathcal{N}_\sigma$ with varying standard deviation $\sigma = 1 : 1 : 5$ pixels was added to the image points. For this set the amount of deformation was set to $\epsilon = 15\%$. *(ii)* Robustness to amount of deformation: deformations in the range $\epsilon = \{2\%,\ 5\%,\ 7\%,\ 10\%,\ 12\%,\ 15\%\}$ are tested

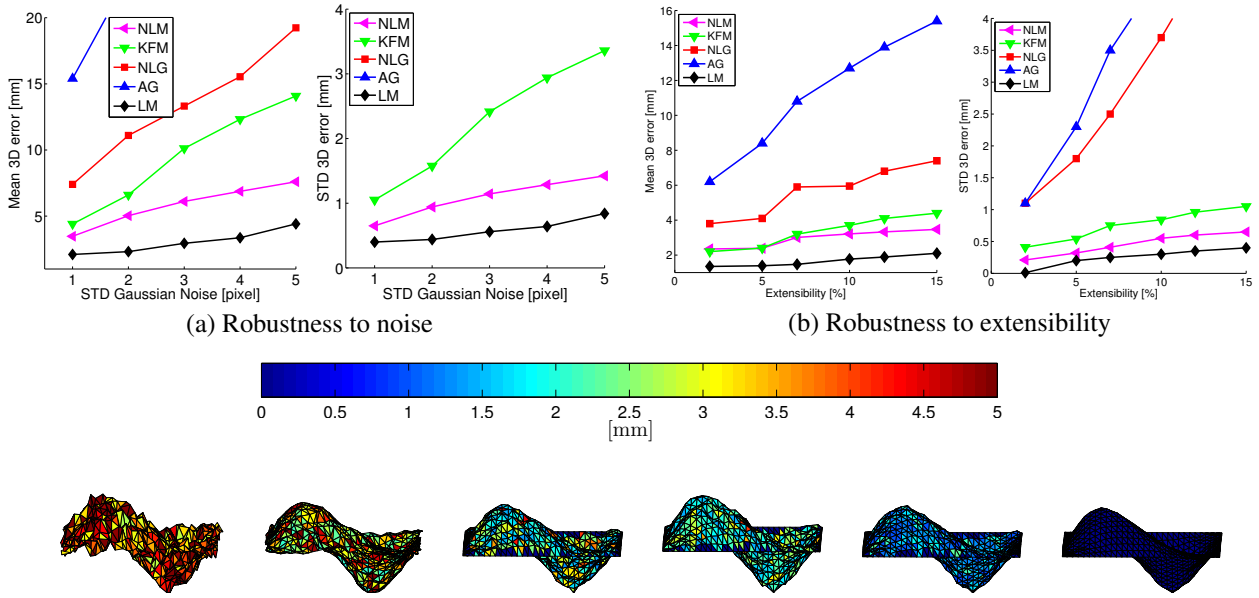

(a) Robustness to noise

(b) Robustness to extensibility

(c) 3D Reconstructions with error display ($\epsilon = 15\%$, $\sigma = 1$). From left to right: **AG, NLG, KFM, NLM, LM** and ground-truth.

Figure 3. Results on simulated deformations. Large error results are not displayed to fit the error scale of the most accurate methods.

with image noise $\mathcal{N}_1$. We measure the reconstruction accuracy as being the 3D residual error in mm between the ground-truth and the reconstructed 3D points. For each extensibility ratio ϵ and noise $\mathcal{N}_\sigma$, we compute the mean and the standard deviation (std) of the 3D residual error over 100 samples.

The results are shown in figure 3: figures 3-a and 3-b show the error curves while 3-c shows some example of reconstructions. Globally, the error increases when noise or extensibility increase. Also we can notice that methods with mechanical priors outperform methods with geometric priors. Some error values of the latter methods are not displayed in cases where there is at least an order of magnitude difference when compared to the former methods. **NLM** and **KFM** have similar orders of magnitude errors when compared to our proposed method **LM**. However, **LM** is more accurate and more stable than the two other mechanical based methods. **NLM** requires an initial deformed rough shape and an optimal hyper-parameter setting to provide the best possible result. **KFM** is particularly sensitive to noise since it is sequentially integrated from deformation to deformation in the Kalman filter. Moreover, it is worth noting that for such methods, any mismatch defeats the whole procedure that needs to be re-initialized. **LM** is conceptually free from these drawbacks; no hyper-parameter, no initialization and frame independence since it requires an independent single view at each time. These specificities make the **LM** method more appropriate for substantial noise or extensibility. Regarding the computational time, table 2 reports the execution time that we obtained on our platform. The analytic method is with no doubt the fastest. The non-linear iterative methods are the slowest. The proposed method is in the same order of speed as **KFM**. The speed of execution of the **LM** method can be significantly improved if we would take into account the block-wise structure of $\mathbf{K}$.

Method	**NLM**	**KFM**	**NLG**	**AG**	**LM**
Time [sec]	10.6	1.4	10.4	0.5	1.1

Table 2. Execution time for the compared methods. The mentioned values do not take into account the matching process.

8.3. Real Data

For validation with real data, we used four sets of data with ground-truth that was obtained with stereo calibrated cameras [10]. The two cameras have a resolution of 640×480 pixels. A set of 10 deformed shapes was used for each dataset. *(1)* A stretchable **redchecker** pattern clothes made of polyester ($\nu = 0.3$, $E = 10^5$ Pa) with thickness $h = 2$ mm and square size 400×400 mm^2. *(2)* A dotted black/white pattern **spandex** ($\nu = 0.5$, $E = 10^4$ Pa) with thickness $h = 1.5$ mm and square size 400×400 mm^2. *(3)* A **balloon** pattern fabric made of rubber ($\nu = 0.5$, $E = 10^3$ Pa) with $h = 0.7$ mm and bounding box $150 \times 150 \times 100$ mm^3. *(4)* a **cap** made of quasi-inextensible polyester material ($\nu = 0.001$, $E = 10^7$ Pa) with $h = 2$ mm and bounding box $220 \times 220 \times 150$ mm^3. The **redchecker** and **spandex** materials are clipped on the edge of a box to fixed boundary for the *SBC*. The balloon is clipped to a cup-ring in order to fix its boundaries. The cap was deformed only in the top of the cap so that its surroundings are kept rigid. The boundary points were estimated by a PnP method [14][1]. Features are

[1] http://cvlab.epfl.ch/software/EPnP/index.php

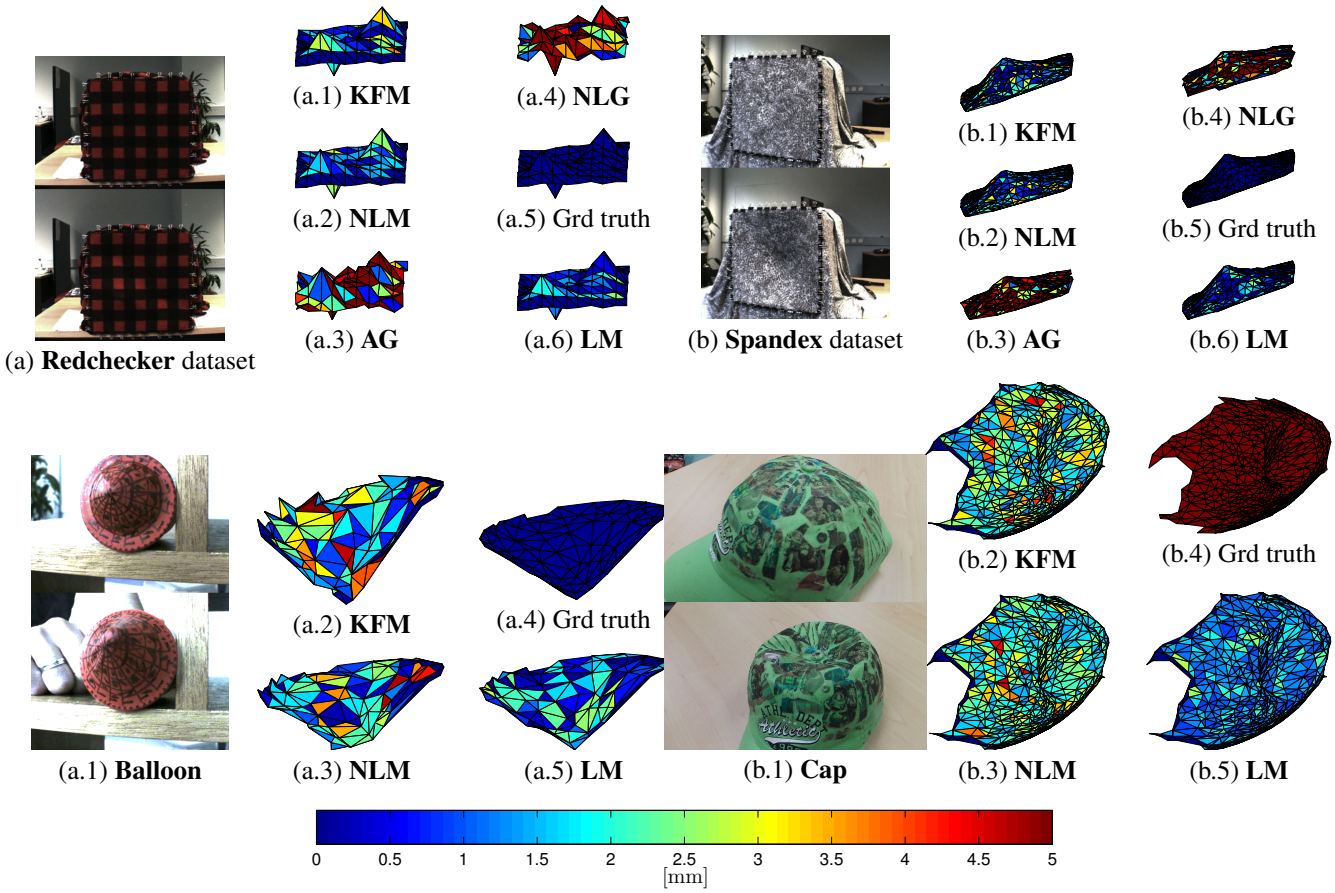

Figure 4. 3D reconstructions of real datasets. The ground-truth of the **cap** data is shown in red for better display.

obtained semi-automatically with SIFT [8]. For the **redchecker** pattern, its corner points were used for manual-driven point selection. A total of 100 feature points and 36 fixed boundary points were used for this dataset. For the **spandex**, features are found by manual selection with initial matches from SIFT. A total of 212 feature points and 45 fixed boundary points were used for this dataset. For the **balloon** a total of 95 feature points and 30 fixed boundary points were used for this dataset. A set of 40 boundary points and a 130 point correspondences were used for the **cap**. These feature points are used as nodes of the mesh. The extensibility ranges from 0% to 15% for the whole dataset except for the cap for which it was negligible. The mean 3D error was measured at about 1 mm for **LM**, 1.3 mm for **NLM** method, 1.7 mm for **KFM**, 5.3 mm for **NLG** and 6.9 mm for **AG**. Table 3 gives more details about the mean and std of 3D errors.

Method	NLG	AG	NLM	KFM	LM
redchecker	4.5/3.5	5.7/3.6	1.2/1.0	1.3/1.2	0.9/0.8
spandex	5.0/3.6	6.2/4.1	1.4/1.1	1.4/1.3	1.1/0.9
balloon	7.5/5.9	8.7/5.5	1.8/1.5	2.0/1.5	1.2/1.0
cap	3.0/2.5	3.7/2.9	1.4/1.0	1.3/1.2	0.9/0.6

Table 3. Average and standard deviation of 3D error (in mm) for the real datasets.

9. Conclusion

We formulated SfT as finding the deformation field through linear least-squares using mechanical priors. To obtain this result we minimized the norm of the deforming forces subject to reprojection boundary conditions and some solid boundary points. We showed experimentally that this method is more accurate than state-of-the-art methods, computationally efficient and has the fundamental advantage of being convex. It opens perspectives for real time SfT in critical applications in the medical field for instance. We think that image matching under elastic deformations is an interesting area of future research.

Acknowledgements

This research has received funding from the EU's FP7 through the ERC research grant 307483 FLEXABLE.

References

[1] A. Agudo, B. Calvo, and J. Montiel. FEM models to code non-rigid EKF monocular SLAM. *IEEE*

Workshop on Dynamic Shape Capture and Analysis of ICCV, 2011. 1, 2, 6

[2] A. Agudo, B. Calvo, and J. Montiel. Finite element based sequential bayesian non-rigid structure from motion. *CVPR*, 2012. 1, 2

[3] A. Bartoli, Y. Gérard, F. Chadebecq, and T. Collins. On template-based reconstruction from a single view: Analytical solutions and proofs of well-posedness for developable, isometric and conformal surfaces. *CVPR*, 2012. 1, 2, 6

[4] A. P. Boresi, R. J. Schmidt, and O. M. Sidebottom. *Advanced Mechanics of Materials*. Wiler, 1993. 3, 5

[5] F. Brunet, R. Hartley, A. Bartoli, N. Navab, and R. Malgouyres. Monocular template-based reconstruction of smooth and inextensible surfaces. *ACCV*, 2010. 1

[6] J. Chaskalovic. *Finite Elements Methods for Engineering Sciences*. Springer Verlag, 2008. 5, 6

[7] N. Haouchine, J. Dequidt, M.-O. Berger, and S. Cotin. Single View Augmentation of 3D Elastic Objects. *ISMAR*, 2014. 1, 2

[8] D. G. Lowe. Distinctive image features from scale-invariant keypoints. *International Journal of Computer Vision*, 60(2):91–110, 2004. 8

[9] A. Malti, A. Bartoli, and T. Collins. Template-based conformal shape-from-motion from registered laparoscopic images. *MIUA*, 2011. 1, 2, 6

[10] A. Malti, R. Hartley, A. Bartoli, and J.-H. Kim. Monocular template-based 3D reconstruction of extensible surfaces with local linear elasticity. *CVPR*, 2013. 1, 2, 6, 7

[11] M. Matossian. *3D Studio MAX 3: Visual QuickStart Guide*. Peachpit Press, 1999. 6

[12] I. Matthews and S. Baker. Active appearance models revisited. *International Journal of Computer Vision*, 60(2):135–164, November 2004. 1

[13] T. Mcinerney and D. Terzopoulos. Deformable models in medical image analysis: A survey. *Medical Image Analysis*, 1:91–108, 1996. 2

[14] F. Moreno-Noguer, V. Lepetit, and P. Fua. Accurate non-iterative o(n) solution to the pnp problem. *ICCV*, 2007. 7

[15] F. Moreno-Noguer and J. Porta. Probabilistic simultaneous pose and non-rigid shape recovery. *CVPR*, 2011. 1

[16] R. Navaratnam, A. W. Fitzgibbon, and R. Cipolla. The joint manifold model for semi-supervised multi-valued regression. *ICCV*, 2007. 1

[17] M. Salzmann and P. Fua. Reconstructing sharply folding surfaces: A convex formulation. *CVPR*, 2009. 1

[18] M. Salzmann and P. Fua. Linear local models for monocular reconstruction of deformable surfaces. IEEE *Transactions on Pattern Analysis and Machine telligence*, pages 931–944, 2011. 1

[19] M. Salzmann and R. Urtasun. Beyond feature points: Structured prediction for monocular non-rigid 3D reconstruction. *ECCV*, 2012. 1

[20] T. Shen, H. Li, Z. Qian, and X. Huang. Active volume models for 3D medical image segmentation. *CVPR*, 2009. 2